Spin wave excitation, detection and utilization in the organic-based magnet, $V(TCNE)_x$ (TCNE = tetracyanoethylene)

*Haoliang Liu, Hans Malissa, Ryan M. Stolley, Jaspal Singh, Matthew Groesbeck, Henna Popli, Marzieh Kavand, Su Kong Chong, Vikram V. Deshpande, Joel S. Miller, Christoph Boehme, Z. Valy Vardeny**

adma.202002663

Spin waves, quantized as magnons, have been studied for applications in next generation information processing devices. Magnonic materials have low energy loss and magnetic damping that are critical for their practical application for magnonic devices, i.e. devices based on spin-wave propagation. The organic-based magnet [$V(TCNE)_x$; TCNE = tetracyanoethylene; $x \approx 2$] has shown an extremely low magnetic damping comparable to, e.g. yttrium iron garnet (YIG). We demonstrate the excitation, detection and utilization of coherent and non-coherent spin waves on various modes in $V(TCNE)_x$, and show that the angular momentum carried by microwave-excited coherent spin waves in a $V(TCNE)_x$ film can be transferred into an adjacent Pt layer via spin pumping and detected using the inverse spin Hall effect. The spin pumping efficiency can be tuned by choosing different excited spin wave modes in the $V(TCNE)_x$ film. In addition, we show that non-coherent spin waves in a $V(TCNE)_x$ film, excited thermally via the spin Seebeck effect, can be also used as spin pumping source that generates an electrical signal in Pt with a sign change in accord with the magnetization switching of the $V(TCNE)_x$. Combining coherent and non-coherent spin wave detection, the spin pumping efficiency can be thermally controlled, and new insight is gained for the spintronic applications of spin wave modes in organic-based magnets.

* Dr. H. Liu, Dr. H. Malissa, J. Singh, Dr. M. Groesbeck, H. Popli, Dr. M. Kavand, S. K. Chong, Prof. V. V. Deshpande, Prof. C. Boehme, Prof. Z. V. Vardeny
Department of Physics & Astronomy
University of Utah
Salt Lake City, UT 84112, USA
E-mail: val@physics.utah.edu

Dr. R. M. Stolley, Prof. J. S. Miller
Department of Chemistry
University of Utah
Salt Lake City, UT 84112, USA

Through the propagation of precessing magnetic moments in magnetic materials, quantized spin waves are efficient information carriers that can be utilized for storage, transmission and processing, enabling the currently strongly investigated emerging technology called *Magnonics*. Compared with conventional electronic devices based on electrical currents, magnonic devices have the advantages of reduced Joule heating dissipation, a broad frequency range, and high tunability through the choice of suitable magnetic materials.[1] Magnonic devices can be driven using different physical mechanisms such as microwave (MW) absorption, thermal gradient, and electrical current, which cause spin pumping,[2] the spin Seebeck effect,[3] and spin transfer/orbit torque,[4] respectively. Moreover, magnonic devices are compatible with conventional electronic devices, i.e., the spin angular momentum carried by a spin wave can be directly converted into a charge current through the inverse spin Hall effect (ISHE).[5,6]

Yttrium iron garnet, $Y_3Fe_5O_{12}$ (YIG) has been demonstrated to be an excellent magnetic material candidate for the fabrication of magnonic devices due to its extremely low magnetic damping (10^{-4}-10^{-5}) and macroscopic spin wave diffusion length.[7] However, practical applications have been limited due the complexity of the critical epitaxial relationship with its only one suitable substrate, namely, gadolinium gallium garnet, $Gd_3Ga_5O_{12}$, and its demanding deposition conditions.[8] Magnetic damping increases by orders of magnitude when thin YIG films and substrates are lattice mismatched. In contrast, the $V(TCNE)_x$ (TCNE = tetracyanoethylene, $x \approx 2$)[9,10] organic-based magnet has been shown to be an alternative candidate for magnonic devices with comparable magnetic damping to YIG, but unlike YIG, it is compatible with many substrates[11] and has forgiving deposition conditions due to its amorphous microscopic nature.[0-13] In the past decade, organic materials have had great successes in spintronic devices, as well as optoelectronic devices.[14-16] Due to their small spin orbit coupling strength, they have shown promising results in spin polarized electron transport,[14] pure spin current transport,[17] spin light emitting diodes,[19] and spin photovoltaics.[19] Recently, new applications of organic materials have been developed for magnonics,[20] energy storage,[21] and quantum computing.[22,23] In particular, the $V(TCNE)_x$ organic-based magnet has been integrated into spin valves and spin light emitting diodes due to its $\lesssim$100% spin polarization at low temperature.[24,25] Various spin wave modes with high quality factors have been observed by spatial confinement of $V(TCNE)_x$ films.[26] The spin current carried by magnons in $V(TCNE)_x$ possesses a long lifetime and low Gilbert damping, and can be converted into an electrical current in an adjacent Pt layer by the ISHE.[12]

In this study, we show that coherent and non-coherent spin waves can be generated in $V(TCNE)_x$ films by microwave irradiation and thermal heating, respectively. We also show that the spin-to-charge conversion efficiency in a $V(TCNE)_x$/Pt bilayer can be effectively controlled by choosing different surface spin wave modes. In addition, we show that the electrical current generated by thermally excited non-coherent spin waves using the spin-Seebeck effect in the organic film follows the trace of magnetization switching in $V(TCNE)_x$. We have thus demonstrated the ability of generating, detecting and utilizing both coherent and non-coherent spin waves in organic-based magnets. This enables new applications of spin waves of organic magnetic materials in spintronics and spin caloritronics.

In $V(TCNE)_x$ the spins of V^{II} ($S = 3/2$) and $(TCNE)^-$ ($S = 1/2$) are antiferromagnetically exchange coupled, as illustrated in **Figure 1**a, which yields ferrimagnetic ordering with a net magnetic moment of ~1 μ_B/molecule that is obtained from the saturation magnetization where μ_B is Bohr magneton. The precession of the net magnetic moment forms spin waves in $V(TCNE)_x$. Depending on the relative orientations of the in-plane magnetic field and the wave vector of the

ferromagnetic resonant drive field, there are two types of propagating spin waves in a $V(TCNE)_x$ slab (see **Figure 1**c and the SI).[27] These are: (i) a magnetostatic surface spin wave (MSSW) with its magnetic field perpendicular to the wavevector, $\boldsymbol{k}$ and (ii) a backward volume magnetostatic wave (BVMSW) with its magnetic field parallel to $\boldsymbol{k}$. **Figure 1**b displays a typical magnetic hysteresis loop of a thin ~220 nm $V(TCNE)_x$ film measured by an ultrasensitive Sagnac magneto-optic interferometer in transmission geometry with 1550 nm radiation at several temperatures.[28] The obtained magnetic coercivity is ~0.5 mT at room temperature, consistent with previous studies utilizing other techniques.[9] Both the coercivity and magnetization significantly increase upon lowering the temperature. The Faraday rotation constant of $V(TCNE)_x$ at 1550 nm is estimated to be 1.4×10^5 deg/(Tm) with the magnetization taken as $M_S = 6.9$ kA/m;[12] which is one order of magnitude larger than that of the ferrimagnetic YIG [1.2×10^4 deg/(Tm), see **Figure S8**].

Figure 2a schematically shows the generation and detection of coherent spin waves using microwave (MW) excitation in $V(TCNE)_x$/Pt in a bilayer device. The excited spin waves propagate towards the $V(TCNE)_x$/Pt interface and transfer spin angular momentum to the Pt layer by spin pumping, causing a pure spin-current away from the interface within the Pt layer. This pure spin current is then converted into a perpendicular electrical current within the Pt layer and parallel to the interface by the ISHE. **Figure 2**b shows the spin wave resonances of the spatially confined $V(TCNE)_x$ film using the magnetic field response of the derivative of the MW absorption at a fixed, continuous wave (cw) frequency of 3.975 GHz. In addition to the main ferromagnetic resonance (FMR) at 138.2 mT, which originates from the uniform mode (wavevector $\boldsymbol{k} = 0$) of the spin waves; there are three additional resonances; two of them occur at lower magnetic fields, and another occurs at a magnetic field above the uniform mode resonance. These spin wave modes with $\boldsymbol{k} \neq 0$ can be attributed to MSSWs and BVMSWs, respectively, derived according to the analytical solution of a spatially confinement $V(TCNE)_x$ thin film (see SI). The wavenumber indices (n, m) correspond to the wavevector components $k_x = \frac{n\pi}{x}, k_y = \frac{m\pi}{y}$, where x, and y are the lateral dimension of the $V(TCNE)_x$ slab. The larger field spacing of BVMSW with respect to MSSW is due to the stronger spatial confinement along the y direction (see the Experimental Section).

Under FMR conditions for the $V(TCNE)_x$ film, spin pumping transfers spin angular momentum is carried by the excited spin waves into the adjacent Pt layer, where an ISHE voltage, V_{ISHE} is generated. **Figure 2**c shows the ISHE(B) response in Pt for a FMR drive MW power of 0.2 mW. Peaks in $V_{ISHE}(B)$ appear at the resonance fields of all the spin wave modes in **Figure 2**b, and they change polarity when the magnetic field direction is reversed. This identifies the ISHE response since $\boldsymbol{j_c} \propto \boldsymbol{j_S} \times \boldsymbol{\sigma}$, where $\boldsymbol{j_c}$, $\boldsymbol{j_S}$ and $\boldsymbol{\sigma}$ are the respective electrical current, spin current and spin polarization vectors of the electrons.[5] **Figure 2**d shows V_{ISHE} as a function of the driving MW excitation power, P. V_{ISHE} increases linearly with P. Remarkably, the slope of this increase is greater for the MSSW than for the uniform mode, causing the maximum of the combined $V_{ISHE}(B)$ spectrum to shift to lower magnetic fields at higher P. **Figure 2**e summarizes the MW power dependencies of V_{ISHE} for the various excited spin wave modes; all modes show a linear relationship with P. As shown in **Figure 2**f, the linear slopes of $V_{ISHE}(B)$ correspond to the spin pumping efficiencies, and are larger for the MSSW and BVMSW compared to the uniform mode; with the higher order MSSW modes having larger spin pumping efficiencies compared to the lower order MSSW modes. The underlying mechanism for this is related to the nature of the excited spin wave modes, where the $\boldsymbol{k} \neq 0$ spin waves are more localized at the layer surfaces/interfaces. It is known that the MSSW amplitude decays away from the layer surfaces/interfaces,[27,29,30] leading

to higher spin angular momentum densities at the surfaces/interfaces for $\boldsymbol{k} \neq 0$ spin wave modes. This explains why the MSSW modes exhibit higher spin pumping efficiencies.

In order to exclude cw microwave radiation induced continuous heat- and heat-gradient related artifacts as the origin of our findings vide supra, we also performed pulsed ISHE measurements (**Figure 3**a),[31] where short, homogeneous, high-power, low-duty cycle (2/16) MW radiation was applied to the magnonic bilayer device; and the generated ISHE current, I_{ISHE} was monitored as a function of time. **Figure 3**b shows a 2D map of $I_{ISHE}(t, B)$ as a function of time, t and magnetic field, B when a 2 μs long microwave pulse at a frequency of 9.63 GHz and amplitude of 0.16 mT was applied to the device. Under these conditions, the high drive field amplitudes correspond, under cw conditions, to significantly higher heating powers. However, due to the low duty cycle, the average device heating is even smaller compared to the cw experiments presented in **Figure 2**.

The horizontal and vertical slice projections in **Figure 3**b correspond to time and magnetic field dependences of I_{ISHE}, respectively, as shown in **Figures 3**c and 3d. An I_{ISHE} signal appears on the same time scale as the MW drive fields in **Figure 3**c. However, the I_{ISHE} maximum in **Figure 3**d broadens and shifts towards lower magnetic field with increasing power. This suggests that the ISHE responses of spin wave modes at lower magnetic field range (i.e., the MSSW) have larger spin pumping efficiencies than the uniform mode; in agreement with the cw spin pumping studies described above. We note that since the lateral slab size in this experiment is ~1 mm, the various spin wave modes are not distinguishable here compared to the cw experiment. However, the shift of $I_{ISHE}(B)$ maximum at higher power still corroborates that different modes respond with different sensitivities to the drive field amplitude.

We note that non-coherent spin waves in $V(TCNE)_x$ may be also excited thermally, as schematically shown in **Figure 4**a. Heating by a laser on one side of the $V(TCNE)_x$/Pt bilayer generates a temperature gradient in the $V(TCNE)_x$ slab perpendicular to the film surface which results in a spin wave density gradient in the organic magnet. Consequently, a spin current occurs along the spin wave density gradient in the $V(TCNE)_x$ slab caused by the longitudinal spin Seebeck effect (LSSE). Upon reaching the $V(TCNE)_x$/Pt interface, the thermally generated spin wave angular momentum may be transmitted to the Pt overlayer where it is converted into an electrical signal, V_{LSSE} in the Pt film, again via the ISHE.[32] **Figure 4**b shows the generated V_{LSSE} response in the Pt overlayer, measured upon irradiation by a 485 nm laser light onto the $V(TCNE)_x$ film at various intensities; this generates variable temperature gradients in the film. We note that the magnetic field direction was in-plane, yet perpendicular to the electrical connection direction in the Pt layer. The $V_{LSSE}(B)$ response shows an excellent correlation with the field response of the $V(TCNE)_x$ magnetization, $M(B)$, that was measured by monitoring the Faraday rotation angle from the film. We also verified that V_{LSSE} in the Pt overlayer disappears when the in-plane magnetic field is parallel to the direction of the electrical connection direction in the Pt film **(Figure S4)**, in accordance with LSSE results in other systems.[33]

Figure 4c displays V_{LSSE} in the Pt layer as a function of the temperature gradient in the $V(TCNE)_x$ film, which, in turn, is controlled by the laser illumination power. The temperature gradient was estimated using a theoretical model (see **Figure S5**).[34] The temperature gradient dependence is in good agreement with a linear function revealing an LSSE induced ISHE coefficient in the Pt film of $\gamma_{OFM}^{LSSE} = \frac{V_{LSSE}}{\Delta T} \sim 11 \pm 4$ nV/K. As a control experiment, we also measured V_{LSSE} in a YIG/Pt bilayer due to LSSE generated in a 30 nm YIG layer prepared by

magnetron sputtering covered with the same Pt thickness as in our $V(TCNE)_x$/Pt bilayer, as shown in **Figure S5**. The $V_{LSSE}(B)$ response also follows the magnetic hysteresis loop of $M(B)$ in the YIG film when sweeping the magnetic field (**Figure S8**). From this we estimated the LSSE related ISHE coefficient in the YIG/Pt bilayer to be $\gamma_{YIG}^{LSSE} \sim 30 \pm 5$ nV/K.

To further explore the spin wave excitations in $V(TCNE)_x$, coherent and non-coherent spin waves were simultaneously generated by the simultaneous application of a thermal gradient and MW radiation to the $V(TCNE)_x$/Pt bilayer. **Figure 5**a shows the schematics of this experiment. The $V(TCNE)_x$/Pt bilayer was continuously exposed to MW radiation from one side, while positive and negative temperature gradients were simultaneously generated from the other side using a Peltier element.[35] In this case both coherent and non-coherent spin waves are generated and converted into an electrical current in the Pt layer by the ISHE. **Figure 5**c shows FMR spectra with positive and negative temperature gradients between the MW source and the Peltier element. In this arrangement the temperature gradients were calibrated by two thermocouples. The resonance shifts to higher field with a positive temperature gradient indicating the decrease of magnetization of $V(TCNE)_x$. This is consistent with magneto-optic measurements in **Figure 1**b as well as the magnetization measurement in **Figure 5**b. Both the ISHE responses of the uniform and MSSW modes change when different temperature gradients are applied. Although the magnetization decreases with increasing temperature, the voltage, V_{ISHE} still increases. Interestingly, a temperature gradient across the $V(TCNE)_x$/Pt bilayer can either add or subtract spin current superimposed on the spin current generated by the MW excitation. Therefore, the magnetic loss and spin-to-charge conversion during the spin pumping process can be tuned by the LSSE in $V(TCNE)_x$/Pt. This points to the possibility that noncoherent spin waves can be used to tune the signal output in MW driven spintronic devices. **Figure 45**d presents a plot of the resonance field, B_R and V_{ISHE} by the uniform spin wave mode as a function of the temperature gradient. The LSSE coefficient of $\gamma_{OFM}^{LSSE} \sim 13 \pm 3$ nV/K has been obtained from a linear fit, and it is in accord with the value discussed earlier.

In summary, both coherent and non-coherent spin waves have been generated in thin-films of the $V(TCNE)_x$ organic-based magnet. These spin waves have been detected through the ISHE via FMR spin pumping and the spin Seebeck effect, respectively. Spin wave modes with $\boldsymbol{k} \neq 0$ in the $V(TCNE)_x$ slab, achieved by lateral confinement, show higher spin pumping efficiencies compared with the uniform mode at $\boldsymbol{k} = 0$. LSSE induced ISHE in the Pt overlayer has been observed by applying a temperature gradient across the $V(TCNE)_x$/Pt bilayer with coefficient $\gamma_{OFM}^{LSSE} \sim 10$ nV/K. In addition, the spin pumping efficiency by MW excitation in the $V(TCNE)_x$ film can be effectively controlled thermally. These results suggest that higher order spin wave modes in $V(TCNE)_x$ films could open up pathways for the application of $V(TCNE)_x$ film in spintronics, spin-caloritronics, and magnonic applications.

Experimental Section

The $V(TCNE)_x$ thin films were prepared by a homebuilt chemical vapor deposition through the reaction of TCNE and $V(CO)_6$ as previously reported,[11] and further details are supplied in the SI. The films had a high FM critical temperature, $T_c \sim 370$ K, a relatively small saturation field (~ 1 mT), and very narrow FMR line width (~ 0.3 mT at 3 GHz). The film thickness was calibrated by profilometry measurements (KLA Tencor). The lateral size of the film is confined by shadow mask during deposition. For the $V(TCNE)_x$/Pt bilayer device, prior to the $V(TCNE)_x$ film deposition, a 7 nm thick Pt layer was deposited on glass substrate for the detection of the ISHE voltage. The

resistance of the Pt layer was ~500 Ω for all the ISHE devices. The electrodes were prepared by photolithography method. The metal depositions were done by electron beam evaporation at a base pressure of 1×10^{-10} bar. Since the $V(TCNE)_x$ film can completely degrade in air within ~2 hr, it was essential to encapsulate the films with a UV cured epoxy [Ossila, Inc. (type E132)], which could significantly increase the film lifetime to more than one month, if stored at low temperature.[36] The YIG films were made as previously reported.[8]

The magnetization, *M* as a function of temperature, *T*, was measured at 100 mT using a Quantum Design MPMS-5 5 T SQUID magnetometer. The magneto-optic Faraday rotation was measured by a modified fiber Sagnac interferometer operating at 1550 nm, which has a Faraday rotation angle resolution of ~20 nrad.[28]

The broadband ferromagnetic resonance (FMR) measurements took place at room temperature with coplanar waveguide setup. The microwave radiation was generated using an Agilent N5173B generator operating in a frequency range of 9 kHz-20 GHz. For the FMR detection we used a phase-sensitive scheme in which a weak magnetic field of 0.2 mT was modulated at 86 Hz in a Helmholtz coil between the poles of the DC magnet.

For the cw inverse spin Hall effect (ISHE) measurements, the MW power was amplified using an amplifier (Mini-Circuits Lab Model ZHL-42). A phase sensitive lock-in detection was used to measure the induced electrical voltage on the Pt layer, and the excitation MW beam was amplitude modulated at 17 kHz. [37]

The pulsed ISHE was measured in a commercial EPR spectrometer (Bruker ElexSys E580). The transient ISHE response during high power MW excitation was measured by a Standard Research Systems SR570 current amplifier using the built-in 100 Hz high pass filter and has a sensitivity of 20 μA/V, and recorded using the SpecJet digitizer.

The spin Seebeck effect (SSE) measurements were performed at 300 K with optical windows (Cryocooler Model SRDK-205). The temperature gradient was generated with a blue (485 nm) cw laser uniformly focused on the Pt stripe using a cylindrical lens. The ISHE-related electrical voltage was detected by Keithley 2182a voltmeter.

ORCID

Christoph Boehme: 0000-0001-7323-5757
Joel S. Miller: 0000-0001-5743-832
Z. Valy Vardeny: 0000-0002-2298-398X
H. Malissa: 0000-0002-5964-3225
Haoliang Liu: 0000-0002-1606-1858

Supporting Information

Supporting Information is available from the Wiley Online Library or from the author.

Acknowledgements

We thank T. Liu and M. Wu (Colorado State University) for the YIG films. This work was supported by the NSF EAGER grant DMR 1836989 (MW induced spin pumping and LSSE), and the MURI-AFOSR grant FA9550-14-1-0037 (device fabrication and FMR measurements).

Conflict of Interest

The authors declare no conflict of interest.

Keywords

Magnonics; organic-based magnet; spin waves; inverse spin Hall effect; organic spintronics.

References:

[1] A. V. Chumak, V. I. Vasyuchka, A. A. Serga, B. Hillebrands, *Nat. Phys.* **2015,** *11*, 453-461.

[2] Y. Tserkovnyak, A. Brataas, G. E. W. Bauer, *Phys. Rev. Lett.* **2002,** *88*, 117601.

[3] K. Uchida, S. Takahashi, K. Harii, J. Ieda, W. Koshibae, K. Ando, S. Maekawa, E. Saitoh, *Nature* **2008,** *455*, 778-781.

[4] M. Collet, X. de Milly, O. d'Allivy Kelly, V. V. Naletov, R. Bernard, P. Bortolotti, J. Ben Youssef, V. E. Demidov, S. O. Demokritov, J. L. Prieto, M. Muñoz, V. Cros, A. Anane, G. de Loubens, O. Klein, *Nat. Commun.* **2016,** *7*, 10377.

[5] E. Saitoh, M. Ueda, H. Miyajima, G. Tatara, *Appl. Phys.s Lett.* **2006,** *88*, 182509.

[6] K. Ando, S. Takahashi, J. Ieda, Y. Kajiwara, H. Nakayama, T. Yoshino, K. Harii, Y. Fujikawa, M. Matsuo, S. Maekawa, E. Saitoh, *J. Appl. Phys.* **2011,** *109*, 103913.

[7] Y. Kajiwara, K. Harii, S. Takahashi, J. Ohe, K. Uchida, M. Mizuguchi, H. Umezawa, H. Kawai, K. Ando, K. Takanashi, S. Maekawa, E. Saitoh, *Nature* **2010,** *464*, 262-266.

[8] D. Ellsworth, L. Lu, J. Lan, H. Chang, P. Li, Z. Wang, J. Hu, B. Johnson, Y. Bian, J. Xiao, R. Wu, M. Wu, *Nat. Phys.* **2016,** *12*, 861-866.

[9] J. M. Manriquez, G. T. Yee, R. S. Mclean, A. J. Epstein, J. S. Miller, *Science* **1991,** *252*, 1415-1417.

[10] J. S. Miller, *Polyhedron* **2009,** *28*, 1596-1605.

[11] K. I. Pokhodnya, A. J. Epstein, J. S. Miller, *Adv. Mater.* **2000,** *12*, 410-413.

[12] H. Liu, C. Zhang, H. Malissa, M. Groesbeck, M. Kavand, R. McLaughlin, S. Jamali, J. Hao, D. Sun, R. A. Davidson, L. Wojcik, J. S. Miller, C. Boehme, Z. V. Vardeny, *Nat. Mater.* **2018,** *17*, 308-312.

[13] A. Franson, N. Zhu, S. Kurfman, M. Chilcote, D. R. Candido, K. S. Buchanan, M. E. Flatté, H. X. Tang, E. Johnston-Halperin, *APL Mater.* **2019,** *7*, 121113.

[14] Z. H. Xiong, D. Wu, Z. V. Vardeny, J. Shi, *Nature* **2004,** *427*, 821-824.

[15] C. D. Dimitrakopoulos, P. R. L. Malenfant, *Adv. Mater.* **2002,** *14*, 99-117.

[16] V. A. Dediu, L. E. Hueso, I. Bergenti, C. Taliani, *Nat. Mater.* **2009,** *8*, 707.

[17] S. Watanabe, K. Ando, K. Kang, S. Mooser, Y. Vaynzof, H. Kurebayashi, E. Saitoh, H. Sirringhaus, *Nat. Phys.* **2014,** *10*, 308-313.

[18] T. D. Nguyen, E. Ehrenfreund, Z. V. Vardeny, *Science* **2012,** *337*, 204-209.

[19] X. Sun, S. Vélez, A. Atxabal, A. Bedoya-Pinto, S. Parui, X. Zhu, R. Llopis, F. Casanova, L. E. Hueso, *Science* **2017,** *357*, 677-680.

[20] N. Zhu, X. Zhang, I. H. Froning, M. E. Flatté, E. Johnston-Halperin, H. X. Tang, *Appl. Phys. Lett.* **2016,** *109*, 082402.

[21] C. Wang, D. Liu, W. Lin, *J. Am. Chem. Soc.* **2013,** *135*, 13222-13234.

[22] A. Gaita-Ariño, F. Luis, S. Hill, E. Coronado, *Nat. Chem.* **2019,** *11*, 301-309.

[23] D. R. Candido, G. D. Fuchs, E. Johnston-Halperin, M. E. Flatté, *arXiv*, **2020**, arXiv:2003.04341.

[24] J.-W. Yoo, C.-Y. Chen, H. W. Jang, C. W. Bark, V. N. Prigodin, C. B. Eom, A. J. Epstein, *Nat. Mater.* **2010,** *9*, 638-642.

[25] L. Fang, K. D. Bozdag, C.-Y. Chen, P. A. Truitt, A. J. Epstein, E. Johnston-Halperin, *Phys. Rev. Lett.* **2011,** *106*, 156602.

[26] M. Chilcote, M. Harberts, B. Fuhrmann, K. Lehmann, Y. Lu, A. Franson, H. Yu, N. Zhu, H. Tang, G. Schmidt, E. Johnston-Halperin, *APL Mater.* **2019,** *7*, 111108.

[27] C. W. Sandweg, Y. Kajiwara, K. Ando, E. Saitoh, B. Hillebrands, *Appl. Phys. Lett.* **2010,** *97*, 252504.
[28] H. Liu, R. McLaughlin, D. Sun, Z. V. Vardeny, *J. Physics D: Appl. Phys.* **2018,** *51*, 134003.
[29] R. W. Damon, J. R. Eshbach, *J. Phys. Chem. Sol.* **1961,** *19*, 308-320.
[30] C. Kittel, *Phys. Rev.* **1958,** *110*, 1295-1297.
[31] M. Kavand, C. Zhang, D. Sun, H. Malissa, Z. V. Vardeny, C. Boehme, *Phys. Rev. B* **2017,** *95*, 161406.
[32] K.-i. Uchida, H. Adachi, T. Ota, H. Nakayama, S. Maekawa, E. Saitoh, *Appl. Phys. Lett.* **2010,** *97*, 172505.
[33] G. E. W. Bauer, E. Saitoh, B. J. van Wees, *Nat. Mater.* **2012,** *11*, 391-399.
[34] M. Schreier, A. Kamra, M. Weiler, J. Xiao, G. E. W. Bauer, R. Gross, S. T. B. Goennenwein, *Phys. Rev. B* **2013,** *88*, 094410.
[35] L. Lu, Y. Sun, M. Jantz, M. Wu, *Phys. Rev. Lett.* **2012,** *108*, 257202.
[36] I. H. Froning, M. Harberts, Y. Lu, H. Yu, A. J. Epstein, E. Johnston-Halperin, *Appl. Phys. Lett.* **2015,** *106*, 122403.
[37] H. Liu, D. Sun, C. Zhang, M. Groesbeck, R. Mclaughlin, Z. V. Vardeny, *Sci. Adv.* **2019**, *5*, eaax9144.

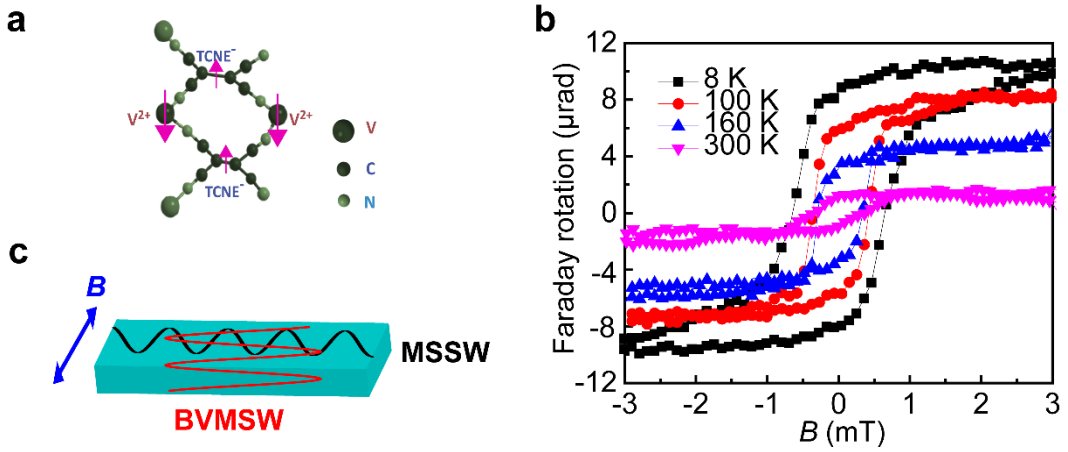

Figure 1. Magnetic properties of the $V(TCNE)_x$ organic-based magnet. a) Proposed nearest neighbor structure and magnetic coupling of $V(TCNE)_x$. b) Magnetic hysteresis loops at various temperatures measured on ~220 nm CVD grown $V(TCNE)_x$ thin film using an ultrasensitive Sagnac magneto-optic Faraday rotation with in-plane magnetic field. c) Schematics of spin wave modes due to spatial confinement of a $V(TCNE)_x$ slab. The spin wave mode is termed the magnetostatic surface wave (MSSW) when the applied in-plane magnetic field is perpendicular to the wavevector, ***k***, whereas it is termed the backward volume magnetostatic wave (BVMSW) when the applied in-plane magnetic field is parallel to the wavevector.

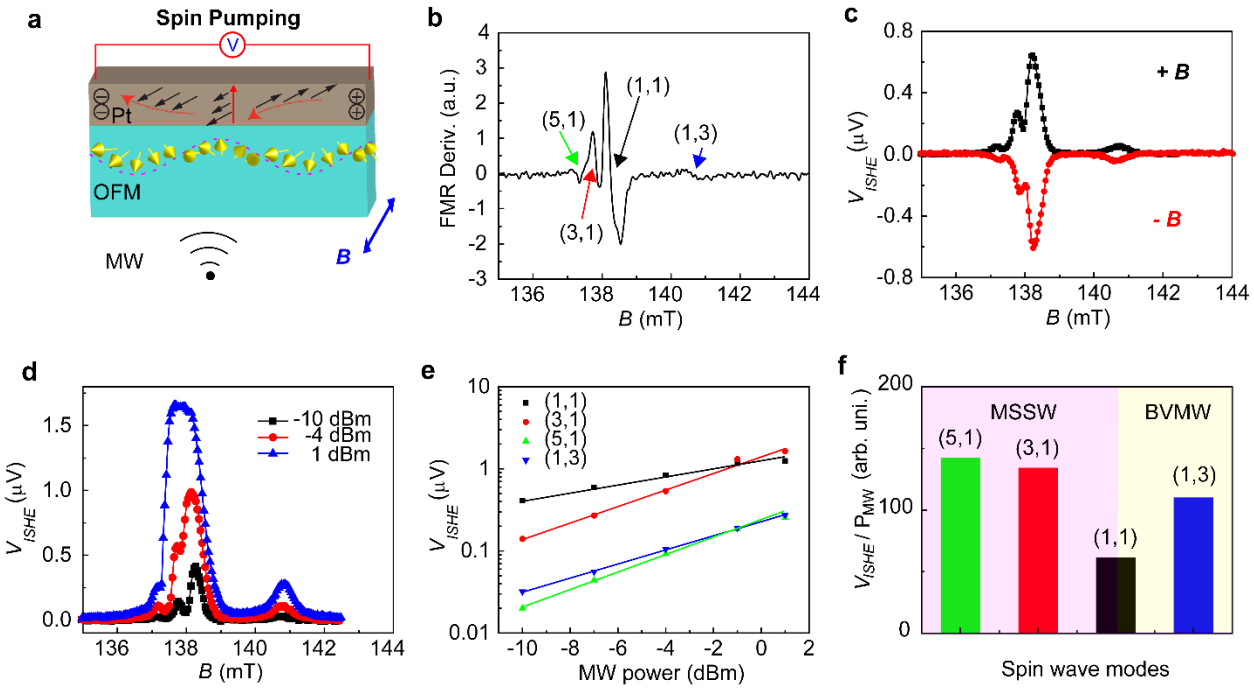

Figure 2. Spin pumping into Pt via excited spin waves in a $V(TCNE)_x$ organic-based magnetic thin film. a) Schematic of the spin wave induced spin pumping process in the $V(TCNE)_x$/Pt bilayer (OFM = organic-based ferrimagnet). b) FMR detection of spin wave resonances of a ~500 nm thin $V(TCNE)_x$ layer grown on a 7 nm Pt layer measured by co-planar waveguide at MW excitation of 3.975 GHz. The lateral size of the $V(TCNE)_x$ thin film is 100×50 μm obtained by a shadow mask during deposition. The resonance field of the uniform mode is 138.2 mT. The resonance fields of the MSSW modes (3,1) and (5,1) as well as the BVMSW mode (1,3) are 137.8, 137.2, and 140.8 mT, respectively. The identification of the different spin wave modes is based on an analytical solution described in the SI. c) The spectrum of the ISHE-voltage, V_{ISHE} that was generated by spin pumping of various spin wave modes, measured at positive and negative magnetic fields. The MW excitation power is 7 dBm. d) The MW power dependence of the V_{ISHE} excited by various spin wave modes. e) V_{ISHE} of different spin wave modes at various MW powers extracted from the data in d). V_{ISHE} increases linearly with the MW power, with the slope being dependent on the pumping efficiency of individual spin modes. f) Plot of spin pumping efficiencies (ISHE voltages normalized by MW power) of the different spin wave modes showing that spin waves with $\boldsymbol{k} \neq 0$ have larger spin pumping efficiencies than the uniform mode with $\boldsymbol{k} = 0$. MSSW have the largest spin pumping efficiencies, increasing with high order modes.

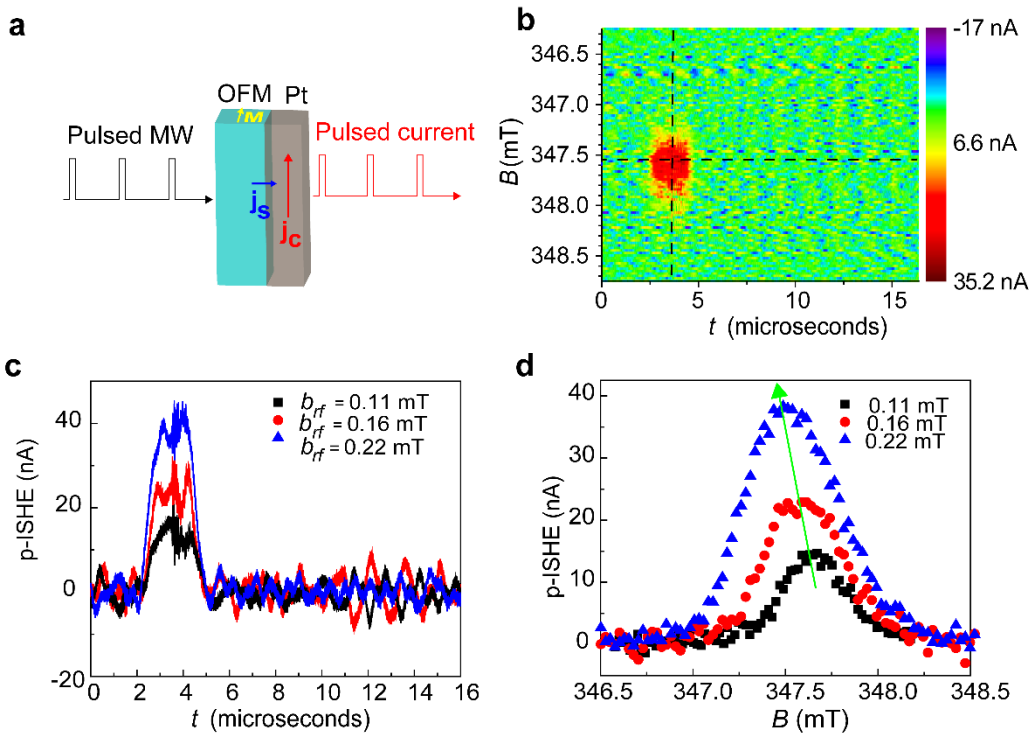

Figure 3. ISHE detected via pulsed spin pumping. a) Schematic of the ISHE current, $\boldsymbol{J}_c$ generated by a pulsed MW excitation. The low duty cycle of the MW pulses suppresses continuous heating artifacts that would be induced under cw MW sources allowing for the application of significantly higher MW power (OFM = organic-based ferrimagnet). The Joule heating is reduced to 1/8 by the pulsed MW compared with the cw measurement at a comparable average MW power. b) 2D map of I_{ISHE} response as a function of time and magnetic field. The lateral size of the $V(TCNE)_x$ film is 1 × 0.5 mm. c) Time dependence of I_{ISHE} measured at a fixed magnetic field [see the horizontal slice in b)] recorded at different pulsed MW powers. All the pulsed ISHE signals appear simultaneously at 2 μs after the pulsed MW excitation. The delay is introduced by the preamplifier in the MW generation setup. The radio frequency field is calibrated accurately by electron paramagnetic resonance.[33] d) Magnetic field dependence of I_{ISHE} response at a fixed time [see the vertical slice in panel b)] recorded at different pulsed MW powers. As emphasized by the green line, with increasing MW power the I_{ISHE} peak shifts towards lower magnetic field due to the enhanced spin pumping efficiencies of the various MSSW modes corroborating the unequal pumping efficiency of the different spin-wave modes. The spin-wave modes with $\boldsymbol{k} \neq 0$ are not resolvable due to the large lateral size of the $V(TCNE)_x$ sample.

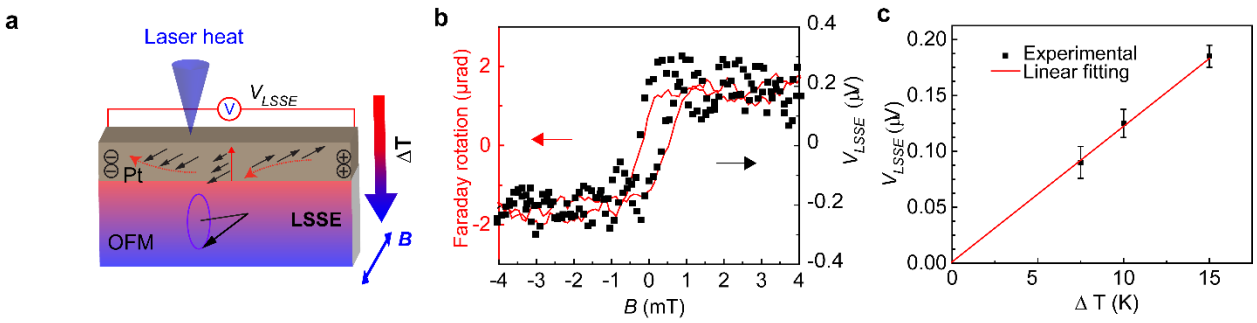

Figure 4. Longitudinal spin Seebeck effect (LSSE) in a $V(TCNE)_x$ organic-based magnet thin-film capped with Pt film. a) Schematic of the LSSE set up in ~ 220 nm $V(TCNE)_x$ grown onto a 7 nm Pt layer. The in-plane magnetic field direction is perpendicular to electrical connection direction. The temperature gradient was generated by 485 nm laser illumination heating with adjustable power, where non-coherent spin waves are excited in the $V(TCNE)_x$ (OFM = organic-based ferrimagnet). b) A typical ISHE response, V_{LSSE} generated in the Pt overlayer via the LSSE in the $V(TCNE)_x$ film when sweeping an in-plane magnetic field, which follows the magnetization switching in the $V(TCNE)_x$ film measured by a Sagnac detected magneto-optic Faraday rotation. c) The temperature gradient dependence of V_{LSSE} in the Pt overlayer, with a linear fit through the data points.

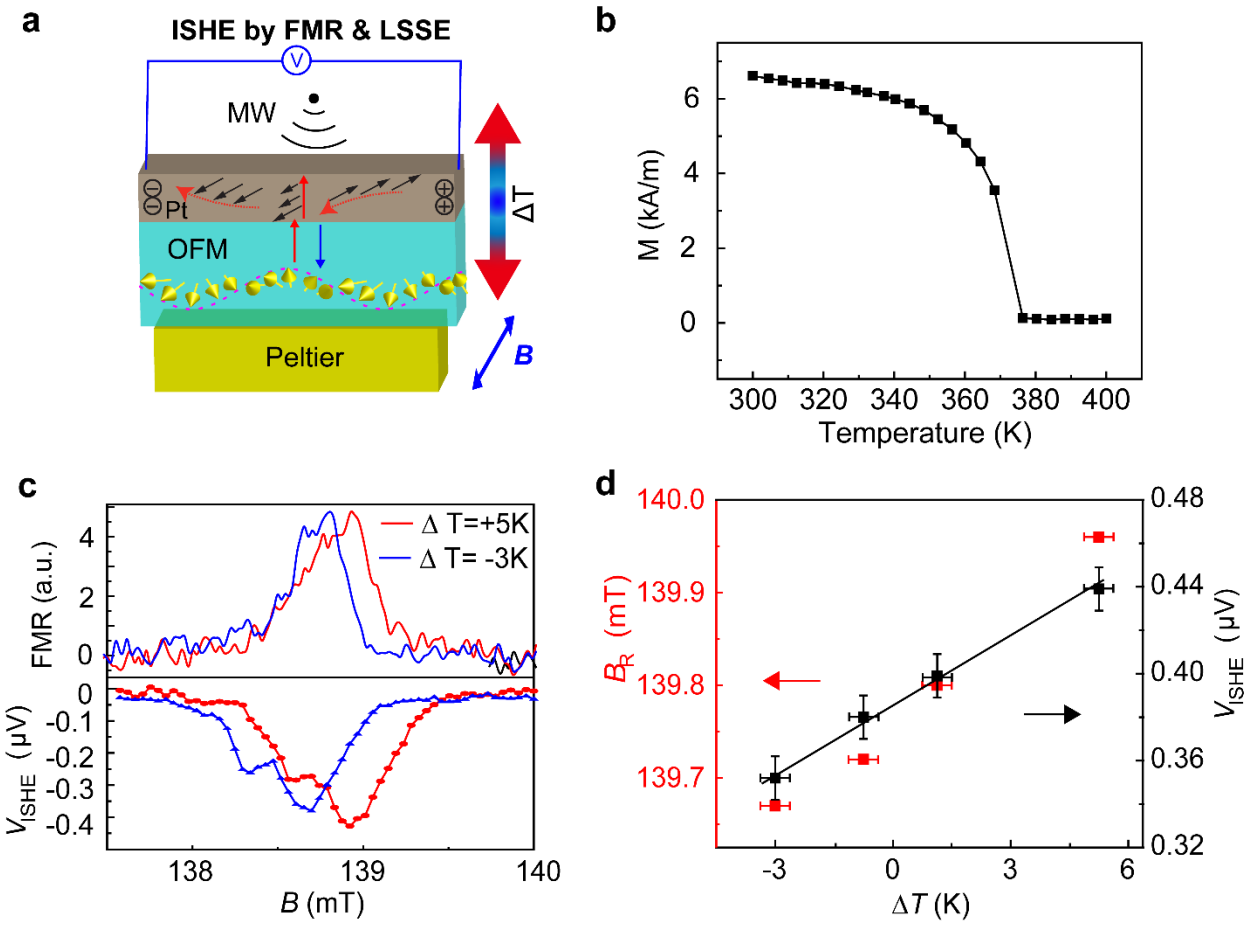

Figure 5. Simultaneous excitation and detection of coherent and non-coherent spin waves in a film of $V(TCNE)_x$ organic-based magnet. a) Schematic of the spin pumping setup due to MW excitation together with LSSE in $V(TCNE)_x$/Pt bilayer (OFM = organic-based ferrimagnet). The microwaves were generated from the lower side of the bilayer by a co-planar waveguide connected with cw microwave source. The temperature gradient was generated by a Peltier system on the upper side. b) The $V(TCNE)_x$ magnetization vs. temperature measured by a SQUID system. c) FMR spin wave resonances (upper panel) and V_{ISHE} responses (lower panel) of a $V(TCNE)_x$/Pt bilayer obtained upon the application of two different temperature gradients, and measured at constant MW excitation power at 4 GHz. d) Resonance fields, B_R, and V_{ISHE} responses of the uniform mode at different temperature gradients. The SSE coefficient can be estimated from the slope of the linear dependence.

Supplemental Information

Spin wave excitation, detection and utilization in the organic-based magnet, $V(TCNE)_x$ (TCNE = tetracyanoethylene)

*Haoliang Li, Hans Malissa, Ryan M. Stolley, Jaspal Singh, Matthew Groesbeck, Henna Popli, Marzieh Kavand, Su kong Chong, Vikram V. Deshpande, Joel S. Miller, Christoph Boehme, Z. Valy Vardeny**

* Dr. H. Liu, Dr. H. Malissa, J. Singh, Dr. M. Groesbeck, H. Popli, Dr. M. Kavand, S. Chong, Prof. V. Deshpande, Prof. C. Boehme, Prof. Z. V. Vardeny
Department of Physics & Astronomy
University of Utah
Salt Lake City, UT 84112, USA.
E-mail: val@physics.utah.edu

Dr. R. M. Stolley, Prof. J. S. Miller
Department of Chemistry
University of Utah
Salt Lake City, UT 84112, USA.

I. Chemical vapor deposition of organic-based magnet $V(TCNE)_x$

Here we give a detailed description of the fabrication method of $V(TCNE)_x$ films by Chemical Vapor Deposition (CVD).

CVD is a process of reacting volatile precursors in a reaction chamber. For CVD deposition of $V(TCNE)_x$ we placed the reaction chamber inside a nitrogen environment. The process involves two precursors that are maintained at different temperatures based on their volatility. The precursors are carried by a carrier gas (Argon) to the reaction zone, where the substrates are kept for thin film deposition. Precursor 1 is Tetracynoethylene (TCNE) that is kept at temperature T_1=55° C whereas Precursor 2 is Vanadium Hexacarbonyl $V(CO)_6$ that is kept at temperature T_2=20° C, as shown in **Fig. S1a**.

Deposition Procedure

- To start the deposition process, we turn on the Argon supply to the Glove Box and setup the reaction chamber.
- We turn on the Heater coil and Cooling Bath PID controller along with the mass flow controller.
- The Argon pressure is maintained at 10 psi before it enters the mass flow controllers.
- The Argon gas goes into two mass flow controllers; one for TCNE and another for $V(CO)_6$ precursor.
- The Argon flow for TCNE is maintained at 100 L/min and for $V(CO)_6$ is 75 L/min
- TCNE is placed in position ② in the figure that is maintained at temperature T_1=55° C.
- $V(CO)_6$ is placed in position ⑤ that is maintained at temperature T_2=20° C.
- The Chamber pressure is maintained 30-35 mmHg.
- The substrates are kept at position ③ that has temperature of 50 - 60 °C.
- The deposition is done for 1 hr for 500 to 700 nm film.
- Once the deposition is done the films are encapsulated using epoxy and cured with UV 365nm for 5 min.
- The films are stored in a refrigerator after encapsulation.

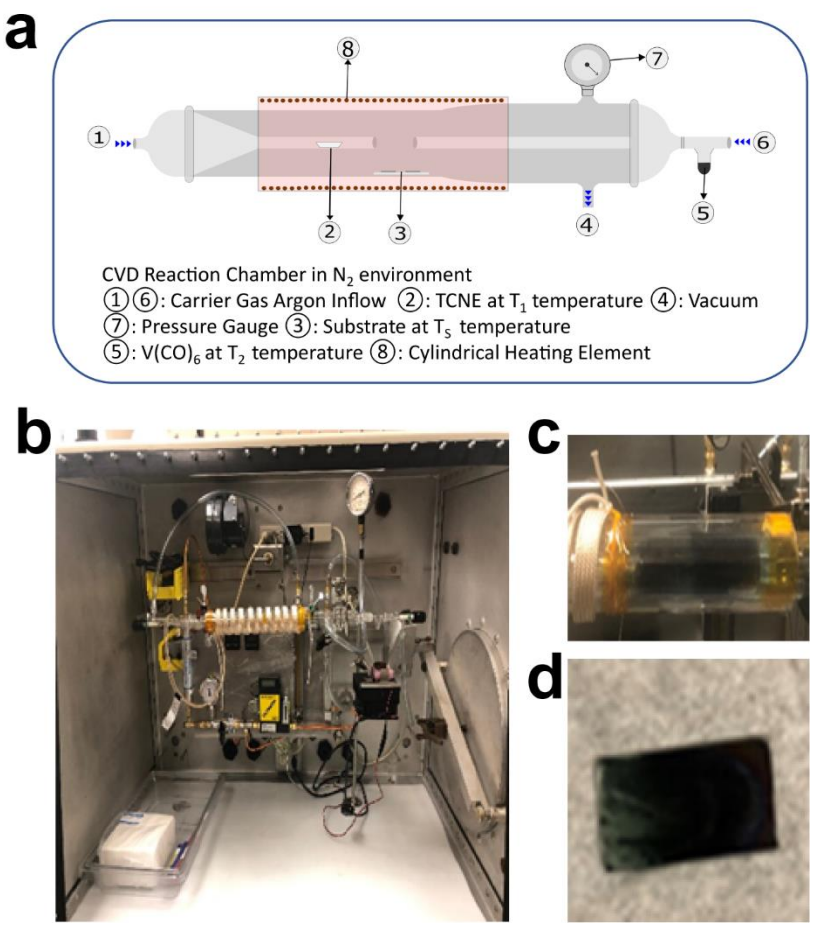

Figure S1. CVD deposition of the $V(TCNE)_x$ organic-based magnet films. **a)** Schematics of CVD setup for $V(TCNE)_x$ thin film preparation. **b)** A photo of the CVD setup integrated in a glove-box filled with pure nitrogen gas. **c)** The enlarged photo of CVD reaction area. **d)** A photo taken of a typical deposited $V(TCNE)_x$ thin film with thickness of ~ 500 nm.

II. Spin wave modes calculation in organic based magnet.

For the uniform ferromagnetic spin wave mode, the wave vector, $\boldsymbol{k}$ is zero. In the case of $\boldsymbol{k} \neq 0$, two different types of spin wave modes are identified. Magnetostatic surface spin waves (MSSWs) is the mode in which the wave vector is perpendicular to the applied in-plane magnetic field. In this case the dynamic magnetization decays away exponentially from the surface. In contrast the backward-volume magnetostatic spin waves (BVMSWs) mode corresponds to the case where $\boldsymbol{k}$ is parallel to the applied DC magnetic field, of which the magnetization dynamics is distributed over the magnetic film thickness, and is small at the surface. Considering that the $V(TCNE)_x$ slab size is 100×50 μm, these two types of spin wave modes are quantized due to lateral and longitudinal confinement, where their dispersion relationship can be described by: [31,32]

$$(1+\alpha^2) + 2|(1+\alpha^2)^{0.5}|(-\frac{1+\alpha^2+\beta}{1+\beta})^{0.5}$$

$$\times (1+\beta)\cot[(-\tfrac{1+\alpha^2+\beta}{1+\beta})^{0.5}|k_y|d] + (1+\beta)^2\left(-\tfrac{1+\alpha^2+\beta}{1+\beta}\right) - \nu^2 = 0, \qquad \textbf{(S1)}$$

where $\alpha = k_x/k_y$, $\beta = \Omega_H/(\Omega_H^2 - \Omega^2)$, $\Omega_H = H_0/(4\pi M_S)$, $\Omega = \omega/(\gamma 4\pi M_S)$, and $\nu = \Omega/(\Omega_H^2 - \Omega^2)$, respectively. Here d is the $V(TCNE)_x$ film thickness, k_x and k_y are wave vector components parallel and perpendicular to the applied DC magnetic field direction. If $1+\beta > 0$, then equation S1 has a solution that corresponds to MSSWs; whereas BVMSWs correspond to $1+\beta < 0$. **Figure S2** shows the calculated spin wave modes dispersion relations based on the $V(TCNE)_x$ sample in Fig. 2 of the text. The MSSW in Fig. 2 are identified as (1, 3), (1, 5), whereas the BVMSW mode is identified as (3, 1). The larger distance between BVMSW and the uniform mode is due to the stronger spatial confinement along the y direction.

Figure S3 shows the spin wave resonances and ISHE responses of ~220 nm thick $V(TCNE)_x$ grown onto 7 nm Pt layer. The spatial confinement is 500 ×100 μm, and thus the MSSW modes are not resolved due to the relatively large film size. **Figure S3(b)** shows the microwave power dependence of the ISHE response, where the maximum position shifts towards lower magnetic field with increasing MW power. Based on the spin wave calculation using Eq. (S1), the resonance field positions of the MSSW can be calculated, as shown in **Fig. S3(c)**. It is seen in **Fig. S3(d)** that the spin pumping efficiency increases for higher MSSW order.

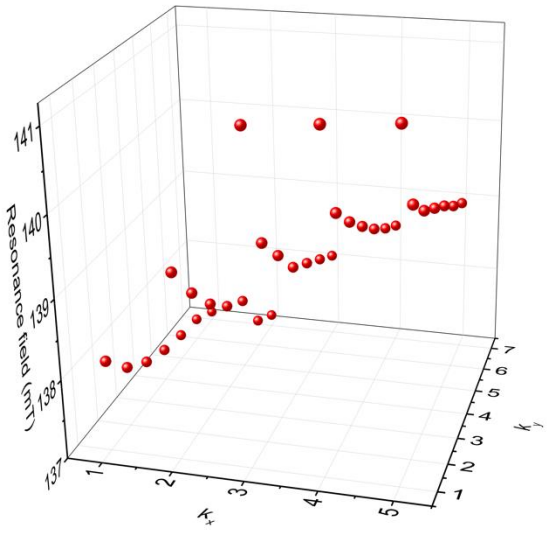

Figure S2. The dispersion relation of spin wave modes calculated based on the spatial confinement of a V(TCNE)$_x$ slab. $k_x = \frac{n\pi}{x}, k_y = \frac{m\pi}{y}$ are wavenumbers along x and y directions, respectively. The microwave frequency is set at 3.975 GHz, as in the experiment described in the text.

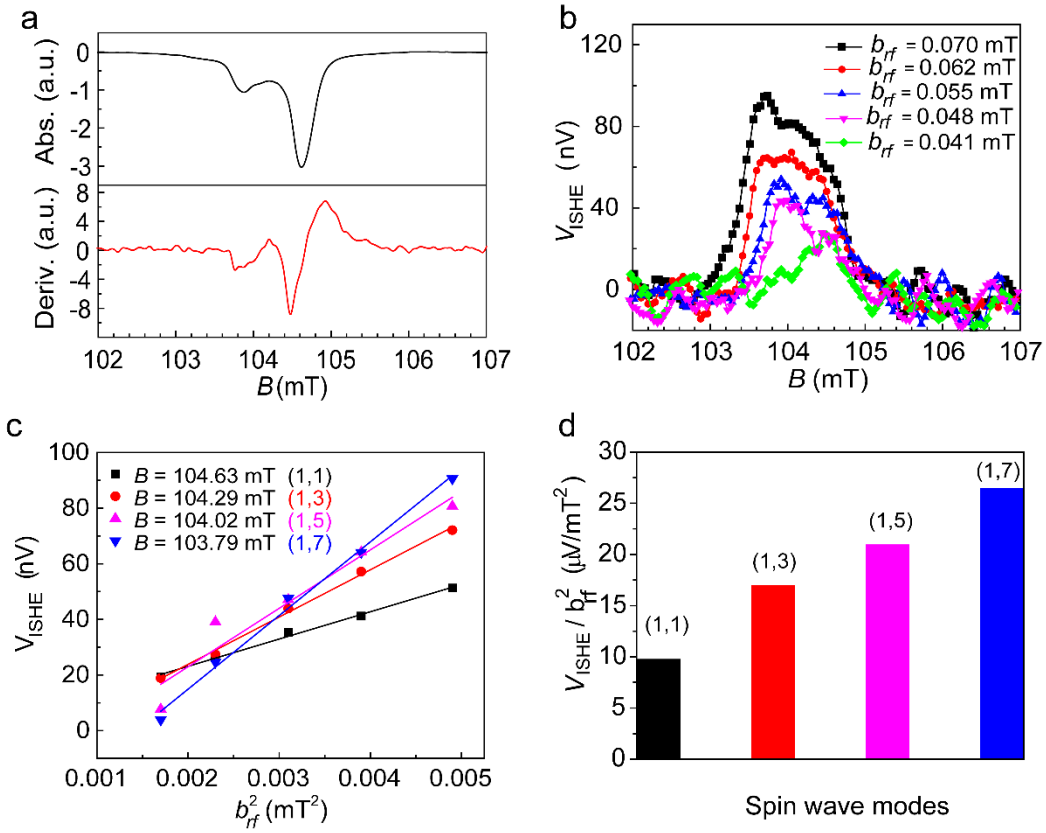

Figure S3. Spin wave induced spin pumping from a ~220 nm thick V(TCNE)$_x$ film grown onto 7 nm Pt layer with spatial confinement of 500 × 100 μm. **a)** Spin wave FMR resonance measured with MW of at 3 GHz, using the first derivative of the microwave absorption (lower panel). The spectrum integration is shown in the upper panel. MSSW spin waves are observed, but the different modes are not resolvable. **b)** The ISHE responses as a function of the MW rf field, b_{rf}. The ISHE voltage, V_{ISHE} increases with increasing rf field strength; remarkably, the main peak is broadened because of the emergent of several new peaks. The maximum of V_{ISHE} response shifts towards lower magnetic field. From the spin wave FMR resonances shown in panel (a) we conclude that V_{ISHE} due to the MSSW modes becomes dominant at larger MW power. **c)** The MW power dependence of V_{ISHE} at magnetic field of 104.63 mT, 104.29 mT, 104.02 mT, and 103.79 mT, respectively, which corresponds to the MSSW modes of n = 1, 3, 5, 7. The ISHE responses of higher order MSSW have stronger linear dependences on the MW power. The slopes of these linear dependences are related to the spin pumping efficiencies of the various spin wave modes. **d)** The spin pumping efficiencies of the various spin wave modes obtained from the slopes in panel (c).

III. Spin Seebeck effect; two control experiments

A control experiment of the LSSE has been done in $V(TCNE)_x$/Pt bilayer with the applied magnetic field **parallel** to Pt stripe, see **Fig. S4**. The measured electromotive force in this case is null, in agreement with the relation $\boldsymbol{j_c} \propto \boldsymbol{j_S} \times \boldsymbol{\sigma}$, where $\boldsymbol{j_c}$, $\boldsymbol{j_S}$ and $\boldsymbol{\sigma}$ are respectively the induced electric current, spin current and spin polarization of electrons.

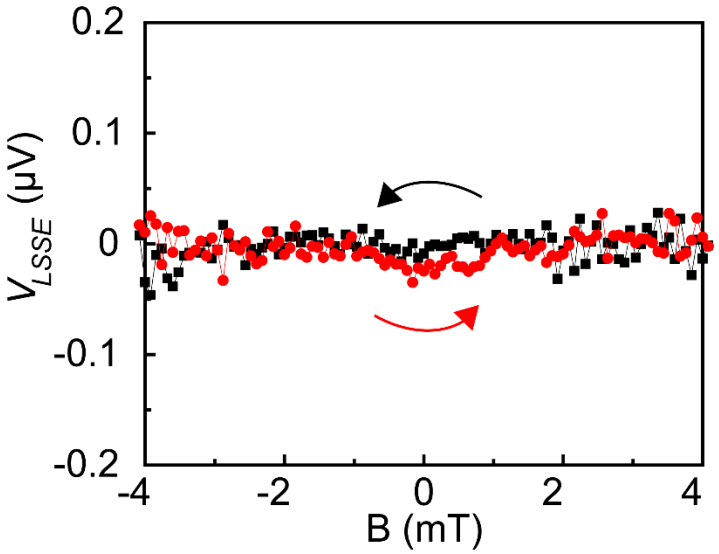

Figure S4. Control experiment of the LSSE. LSSE measurement with applied magnetic field parallel to the Pt stripe for a film of ~220 nm thick $V(TCNE)_x$ grown onto 7 nm Pt film.

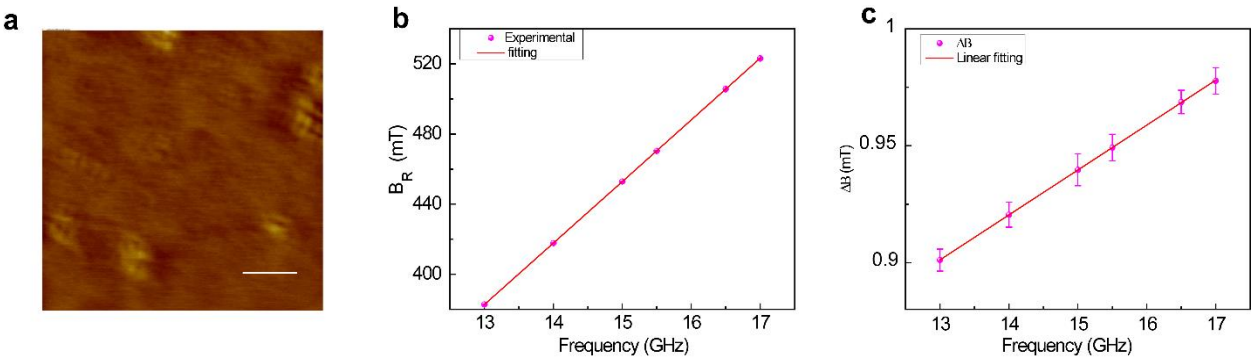

Figure S5. Magnetic properties of 30 nm thick YIG film. **a)** Atomic force microscopy image of YIG thin film. The scale bar is 20 μm and roughness is ~0.2 nm. **b)** and **c)** The microwave

frequency dependence of the resonant fields and linewidth. From these dependencies we estimate that the magnetization is 0.19 T and Gilbert damping (α) is 3.3×10^{-4}.

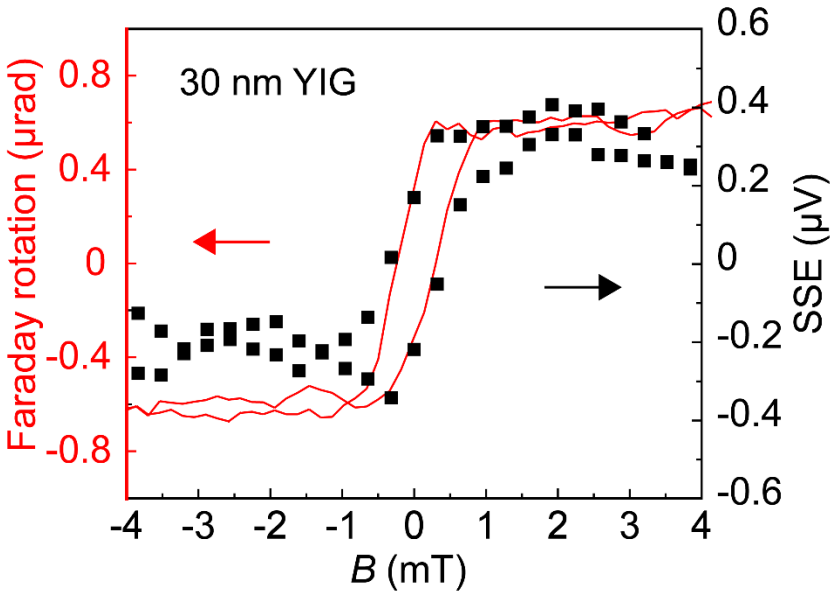

Figure S6. ISHE voltage caused by LSSE in 30 nm YIG thin film on 7 nm Pt layer. The LSSE signal follows the YIG magnetization response. The magnetic hysteresis loop was measured by an ultrasensitive Sagnac interferometer using magneto-optic Faraday rotation.